Acid and Alkaline Dual Stimuli-Responsive Mechanized Hollow Mesoporous Silica Nanoparticles as Smart Nanocontainers for Intelligent Anticorrosion Coatings

JiaJun Fu,[†,§,*] Tao Chen,[†,§] MingDong Wang,[†] NianWang Yang,[†] SuNing Li,[†] Ying Wang,[†] and XiaoDong Liu[‡]

[†]School of Chemical Engineering, Nanjing University of Science and Technology, Nanjing 210094, China, and [‡]School of Environmental and Biological Engineering, Nanjing University of Science and Technology, Nanjing 210094, China. [§]JiaJun Fu and Tao Chen contributed equally to this work.

ABSTRACT The present paper introduces an intelligent anticorrosion coating, based on the mechanized hollow mesoporous silica nanoparticles (HMSs) as smart nanocontainers implanted into the self-assembled nanophase particles (SNAP) coating. As the key component, smart nanocontainers assembled by installing supramolecular nanovalves in the form of the bistable pseudorotaxanes on the external surface of HMSs realize pH-responsive controlled release for corrosion inhibitor, caffeine molecules. The smart nanocontainers encapsulate caffeine molecules at neutral pH, and release the molecules either under acidic or alkaline conditions, which make them spontaneously experience the pH excursions arisen from corrosion process and respond quickly. The intelligent anticorrosion coating was deposited on the surface of aluminum alloy AA2024 and investigated by electrochemical impedance spectroscopy and scanning vibrating electrode technique (SVET). Compared with the pure SNAP coating, the well-dispersed smart nanocontainers not only delay the penetration rate of corrosive species but also repair damaged aluminum oxide layer to maintain the long term anticorrosion behavior. From the experimental results of SVET, the smart nanocontainers with the acid and alkaline dual stimuli-responsive characteristics can simultaneously suppress corrosion activities on microanodic and microcathodic regions, demonstrating an excellent self-healing functionality.

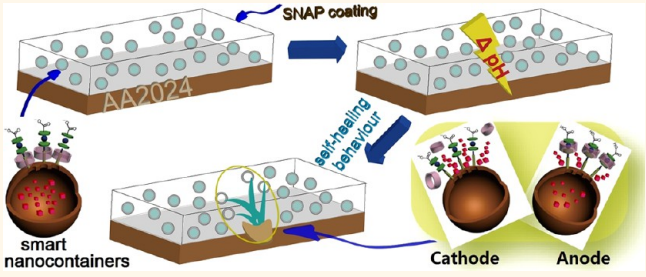

KEYWORDS: mechanized hollow mesoporous silica nanoparticles · dual stimuli-responsive controlled release · smart nanocontainers · supramolecular nanovalves · intelligent anticorrosion coating

Aluminum alloy AA2024 is widely used in the aerospace industry because of its proverbial advantages. However, it is susceptible to the localized corrosion.[1,2] Therefore, it is usually coated pretreatment, primer and top coatings in sequence to enhance corrosion resistance. As a representative of commercial pretreatment coatings, chromate conversion coating, directly deposited on aluminum alloy surface, not only has the excellent paint performance but, more importantly, as the last line of defense, also improves the overall anticorrosion performance on account of its self-healing characteristics.[3] Unfortunately, hexavalent chromium released during the wastewater discharge and waste disposal is extremely toxic, carcinogenic, and environmentally harmful; popularized application of this technology is contrary to the goal of sustainable development.

In the process of finding the qualified alternative for chromate conversion coating, the new design viewpoint of "passive" host-"active" guest coating structures has been proposed and the self-healing property regarded as the core element is taken into account.[4−7] In the cases, the nanocontainers loaded with corrosion inhibitors as coating repair factors have been incorporated into classic passive coatings, and the integrated systems, in which the nanocontainers can sense surrounding environmental changes (*e.g.*, pH,[8,9] temperature,[10]

* Address correspondence to fujiajun668@gmail.com.

Received for review October 12, 2013 and accepted November 21, 2013.

Published online November 21, 2013
10.1021/nn4053233

light,[11,12] aggressive ionic concentration[13]), immediately release corrosion inhibitors to compensate coating defects, providing both the excellent physical barrier effect and self-healing functionality. From the perspective of working mechanism, it is highly desirable to fabricate ideal nanocontainers, which should have two primary features. First, the high loading capacity is required because, once formed, intelligent anticorrosion coatings can hardly receive any supply of coating repair factors.[14] Second, nanocontainers should be endowed with the unique characteristic of "slight stimuli, great response". They should maintain the state of "zero release" under normal condition, while rapidly release corrosion inhibitors after perception of corrosion onset.[15,16] Polyelectrolyte layer-by-layer assembly technique has been adopted to build pH-sensitive shells of nanocontainers to control the release of encapsulated corrosion inhibitors and achieve a significant progress in feedback active anticorrosion coatings.[17−20] However, the operation complexity and premature release weaknesses promote researchers to develop innovations to construct intelligent shells of nanocontainers.[18,21−25]

Since the conception of supramolecular nanovalves was first presented by Stoddart in 2004,[26] a new class of stimuli-responsive controlled release systems, also named mechanized silica nanoparticles, which consist of mesoporous silica scaffolds, cargo molecules, and interlocked molecules as supramolecular nanovalves and are able to respond to all sorts of external stimuli, such as pH,[27−29] redox,[30−32] light,[33,34] and enzyme,[35,36] have sprung up in the past decade. Mesoporous silica nanoparticles functionalized with nanovalves in the form of rotaxanes or pseudorotaxanes to obtain mechanized silica nanoparticles, and the state transition from "close" to "open" of nanovalves depend on the movement of macrocycles noncovalently linked to the axle molecules upon a specific stimulus. With the development of the rotaxane molecular switch assembled by the water-soluble macrocycles, such as cyclodextrin and cucurbit[*n*]uril (CB[*n*]), the use of supramolecular nanovalves extends from organic solvent to water solution, which advances a great breakthrough in targeted delivery of anticancer drugs in biological systems,[37,38] as well as opens the door for application in the field of intelligent anticorrosion coatings. Because the local acidification and local alkalization sites appear continually during corrosion propagation,[23] our research group has successfully introduced the pH-responsive mechanized silica nanoparticles as the active components for intelligent anticorrosion coatings.[39,40] However, the separate fabrication of acid-responsive or alkaline-responsive mechanized silica nanoparticles is time-consuming, laborious and prone to cause virtual waste of coating repair factors due to the uncontrollable distribution of the different functional mechanized silica nanoparticles on appropriate corrosion microregions.

To address this issue and try to get the most out of the mechanized silica nanoparticles, the acid and alkaline dual stimuli-responsive mechanized hollow mesoporous silica nanoparticles have been designed,[41] using hollow mesoporous silica nanoparticles (HMSs) as solid supports and the bistable CB[7]/hexylammonium unit-ferrocenecarboxylic acid unit pseudorotaxanes as supramolecular nanovalves. The selection of HMSs is to multiply the accommodation capacity of corrosion inhibitors. Moreover, the well-designed supramolecular nanovalves can completely encapsulate corrosion inhibitors at neutral pH, and rapidly release molecules either under acidic or alkaline conditions. All these features perfectly match the requirement of the smart nanocontainers for intelligent anticorrosion coatings. In view of this, the mechanized HMSs as smart nanocontainers were uniformly dispersed in the self-assembled nanophase particles (SNAP) coating and subsequently deposited on aluminum alloy AA2024. We focus on the long-term anticorrosion performance of the intelligent anticorrosion coating and the role of the smart nanocontainers in the self-healing process.

RESULTS AND DISCUSSION

Preparation and Characterization of HMSs. The starting HMSs were synthesized in weakly basic ethanol/water solution using relatively concentrated polystyrene latex hard template. Considering the problems of compatibility between the mechanized HMSs and the SNAP coating and the permeability of the mesoporous shell, both the average particle size and the shell thickness are highly regulated. As illustrated in Figure 1A, the scanning electron microscopy (SEM) image shows that the HMSs have a mean diameter of about 100 nm and the spheres are smooth and uniform. The transmission electron microscopy (TEM) image presented in Figure 1B further confirms the hierarchical hollow mesoporous structure with a hollow cavity diameter of 70 nm and a mesoporous shell thickness of 15 nm. Small-angle XRD pattern of HMSs shows one diffraction peak in the 2θ rang $2-3°$, demonstrating the mesoscopic ordering in the shell (shown in Figure 1C). The N_2 adsorption−desorption isotherm of HMSs shows a typical type IV curve with a clear hysteresis loop, indicating the existence of well-defined mesopores (Figure 1D). The BET surface area is 1141.2 $m^2\ g^{-1}$ and the pore volume is 1.07 $cm^3\ g^{-1}$. The pore size distribution (PSD) is narrow and centered at 2.69 nm. The hollow core/thin mesoporous shell structures ensures high loading capacity, and also facilitates corrosion inhibitors easily pass in and out of the HMSs.

Assembling for Mechanized HMSs. The mechanized HMSs are designed herein as smart nanocontainers;

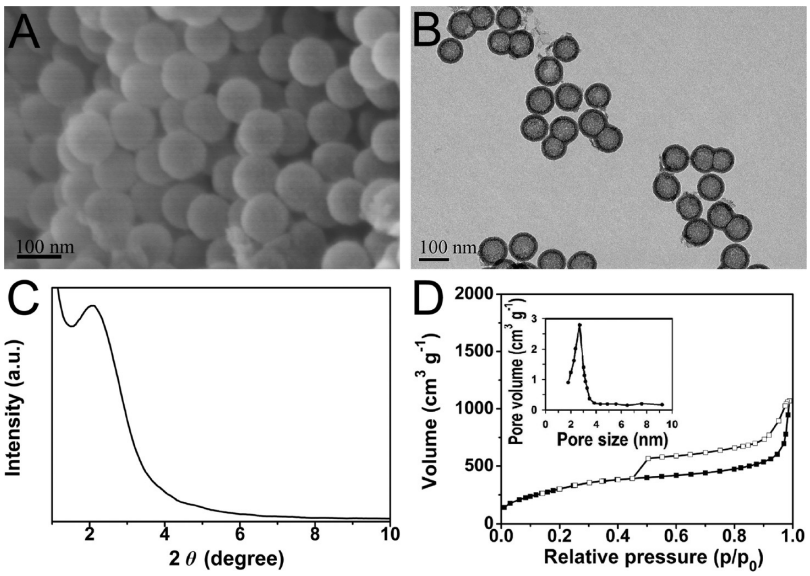

Figure 1. (A) SEM image, (B) TEM image, (C) N_2 adsorption/desorption isotherm and the corresponding pore size distribution, (D) small-angle XRD analysis of HMSs.

their operations mainly depend on the supramolecular nanovalves installed on the external surface of HMSs, which have two vital functions: to prevent any undesirable release under neutral environment and to release inhibitor molecules upon the acid or alkaline stimulus. Typically, the supramolecular nanovalves consist of two constituents, the linear stalks containing the hexylammonium units and the ferrocenecarboxylic acid units linked by amide bonds, and the movable gates, CB[7] macrocycles, which are employed to encircle the stalks to regulate the flow of corrosion inhibitors out of HMSs by moving to the other recogonition sites far away from the pore entrance or leave away from the linear stalks.

Scheme S1 of the Supporting Information shows the schematic illustration of the procedure for assembling the mechanized HMSs. The installation of the linear stalks on the mesopores surface was performed by a three-step surface functionalization process. The bare HMSs were first functionalized with chloromethyltrimethoxysilane (CMTES, HMSs-M1 prepared), subsequently reacted with the excess 1,6-hexanediamine (HAD, HMSs-M2 prepared) in toluene solution, and eventually coupled with ferrocene dicarboxylic acid (FCDCA, HMSs-M3 prepared) to fulfill the whole functionalization process. The assembly of the mechanized HMSs was finalized after loading corrosion inhibitors and capping with CB[7] macrocycles.

The incorporation of the organic stalks inside the framework of HMSs was confirmed by high angle annular dark-field scanning transmission electron microscopy (HAADF-STEM) imaging and EDX spectrometry analysis (see Figure 2). It can be easily seen that the HMSs have good mechanical robustness and are still able to keep morphology mostly unchanged after functionalization. The corresponding elemental mapping images substantiate the existence of well-dispersed Fe and N elements, undoubtedly stemming from the intact stalks. The solid-state NMR experimental results also prove the three-step functionalization process. As can be seen in ^{29}Si SSNMR spectrum of the HMSs-M3 (Figure 3A), the resonance peaks at −109.9, −101.1, and −92.3 ppm can be attributed to Q^4, Q^3, and Q^2 [Q^n = $Si(OSi)_n(OH)_{4-n}$, n = 2−4] silica species. The T signals at −72.1 and −62.8 ppm are assigned to the organosilica T^2 and T^1 species, originating from silicon atoms covalently bonding with the organic substituents (see Figure 3B). The ^{13}C SSNMR spectrum of the HMSs-M3 (Figure 3C) shows the three resonance signals in the aliphatic region from the carbon atoms of hexyl group and methylene group directly bonded to the Si atom. The signals resonating around 68−80 ppm are attributed to the characteristic peaks of cyclopentadienyl. Furthermore, the resonance at 176 ppm is attributed to the carbon atoms of the carboxyl group and the amide group.

Every step of product for assembling the mechanized HMSs was characterized by Fourier Transform Infrared (FTIR). In the FTIR spectra (see Figure S2 of Supporting Information), the pure HMSs show only the surface silanol groups and low-frequency silica vibrations. For HMSs-M1, HMSs-M2 and HMSs-M3, the weak absorption bands at 2956 and 2850 cm^{-1} are observed and assigned to the C−H stretching vibration. The appearance of characteristic N−H bending vibration band at 1485 cm^{-1} and C−N vibration band at 1385 cm^{-1} in HMSs-M2 confirms the connection of HAD.

Moreover, the two new absorption bands at 1680 and 3110 cm^{-1} corresponding to C═O stretching vibration and N−H of amide linkage stretching vibration, respectively, are observed in HMSs-M3, which

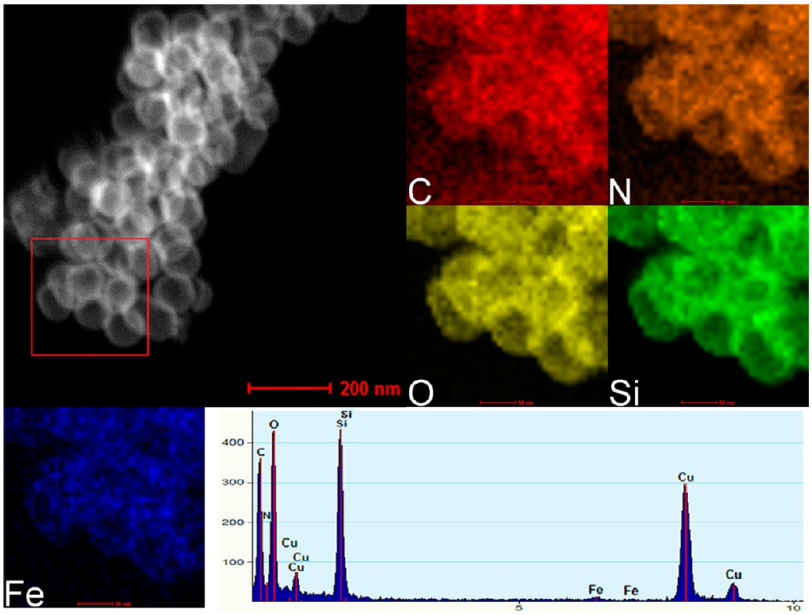

Figure 2. HAADF-STEM and elemental mapping image of HMSs-M3.

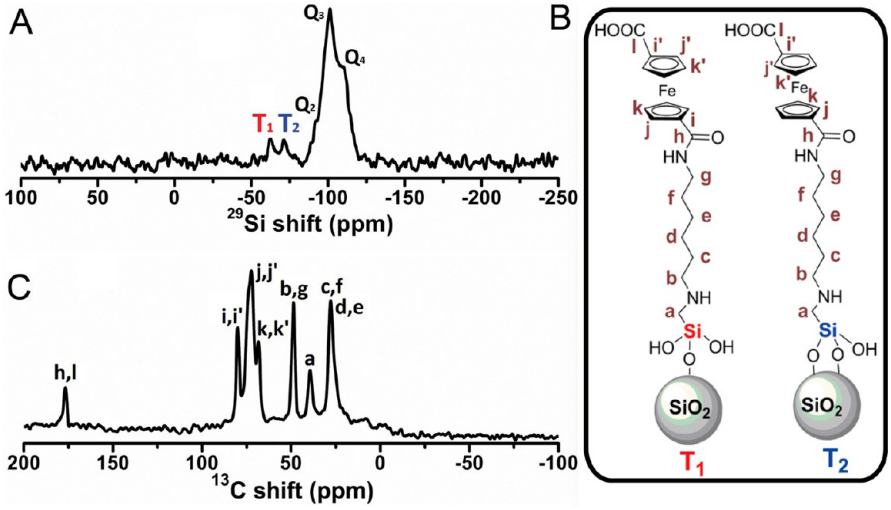

Figure 3. (A) ^{29}Si SSNMR spectrum of HMS-M3, (B) illustration of T region of T^1 and T^2, and (C) ^{13}C SSNMR spectrum of HMSs-M3.

provide clear evidence of grafting the FCDCA groups onto the surface of HMSs. The infrared band at 1730 cm^{-1} in the mechanized HMSs results from the stretching vibration of the carbonyl group of CB[7]. The amount of functional grafted groups can roughly be estimated by thermogravimetric analysis (TGA) and are shown in Figure S3 of Supporting Information. When HMSs are functionalized in sequence with CPTES, HAD, and FCDCA, the relevant total weight loss is about 6.5 wt % (equivalent to 1.3 mmol CPTES g^{-1} HMSs), 8.1 wt % (equivalent to 0.96 mmol HAD g^{-1} HMSs), and 10.1 wt % (equivalent to 0.79 mmol FCDCA g^{-1} HMSs), respectively. It is worthwhile to note that after functionalization, the special surface area, total pore volume and pore diameter somewhat decrease as compared with HMSs (Figure S4 and Table S5 of Supporting Information), but this does not affect the adsorption efficiency. By analyzing the TGA data acquired, the loading capacity of the HMSs-M3 for caffeine molecules is about 20.2 wt %.

Acid and Alkaline Dual Stimuli-Responsive Release Behavior of Mechanized HMSs. According to our initial conception, the working mechanism of the supramolecular nanovalves based on bistable pseudorotaxanes is illustrated in Figure 4A. At near neutral pH environment, CB[7] macrocycles thread onto the hexylammonium recognition site by ion-dipole interaction, acting as gatekeepers and blocking the pore orifices.[42,43] Under this environment, the distal carboxyl groups of ferrocenecarboxylic acid are in the ionization state basically; the strong electrostatic repulsion between the carboxylate anion and the negatively charged carbonyl oxygen

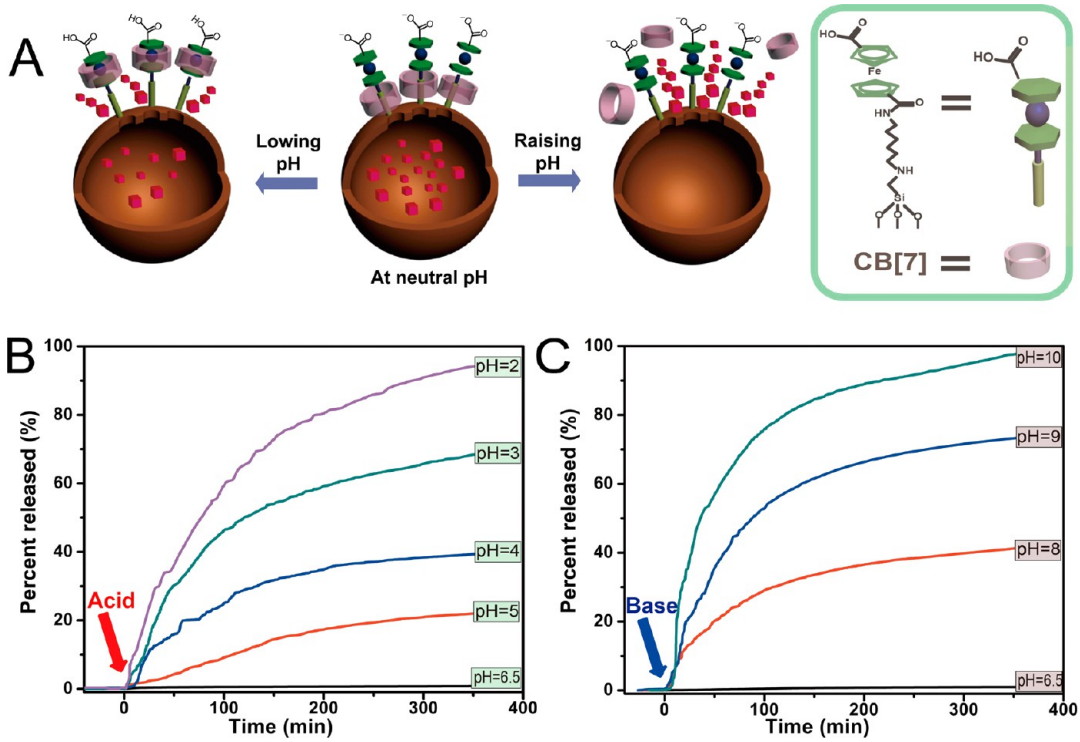

Figure 4. (A) Schematic illustration of the working mechanism for the mechanized HMSs; release profiles of caffeine molecules from the mechanized HMSs under acidic conditions (B) and alkaline conditions (C).

atoms on the portals of CB[7] makes the CB[7] macrocycles unable to reside on the ferrocenecarboxylic acid recognition sites.[30] Upon lowing pH, as the terminal ferrocenecarboxylate anion groups are protonated to some extent, CB[7] macrocycles gradually shuttle toward the ferrocenecarboxylic acid recognition sites because the association constant for the complex between CB[7] and ferrocenecarboxylic acid is much greater than that for CB[7] with hexylammonium.[44] The directional movement of CB[7] macrocycles between the two recogonition sites opens the supramolecular nanovalves and provides pathways for diffusion of corrosion inhibitors. If the pH is elevated, CB[7] macrocycles cannot form stable inclusion complexes either with the deprotonated hexylammonium groups or with ferrocenecarboxylate anion groups, which means the disruption of the structure of the pseudorotaxanes and CB[7] macrocycles will dethread from the stalks, thus leading to the release of corrosion inhibitors from the mesopores.[41]

To verify the design idea and investigate the pH-triggered release of mechanized HMSs, caffeine was employed as cargo. Caffeine is a natural, nontoxic, and environmentally friendly substance and has been used as corrosion inhibitor for a series of metals and alloys owning to its special structure of multiadsorption centers. The Tafel polarization studies in Figure S6 of Supporting Information show that caffeine is a mixed type inhibitor for AA2024 in NaCl solution; both of the anodic and cathodic reactions are obviously suppressed. Figure 4B depicts the release profile of the mechanized HMSs at pH 2, 3, 4, 5, and 6.5 as a function of time. When the pH is 6.5, the UV/vis absorption is negligible and remains more or less unchanged after 6 h, which indicates that caffeine molecules are effectively entrapped in the inner space of the mechanized HMSs by the supramolecular nanovalves. There is already evidence that HMSs with large voids can store more cargoes than those of conventional mesoporous silica nanoparticles;[45,46] however, when HMSs are used as solid supports for controlled release applications, all of the mesopores connected to the hollow interior must be installed nanovalves.[47] Otherwise, an omission in any one of the pores will cause the slow leakage of cargoes. Judging from the experimental data, the supramolecular nanovalves have covered almost all the pore channels of HMSs and achieved "zero premature release" effects. Upon decrease of the pH, a released amount of caffeine molecules considerably increases and the release profiles show two distinct regions: initial burst release region and subsequent sustained release region, indicating that the supramolecular nanovalves are open to the cargoes. The maximum adsorption amount of caffeine molecules in the mechanized HMSs estimated by UV/vis absorption measurement of the supernatant of the sample under pH = 2 after 6 h sonication is about 19.4 wt %, which is slightly less than that determined by TGA measurement due to the partial desorption of caffeine molecules during the capping process. Interestingly, with

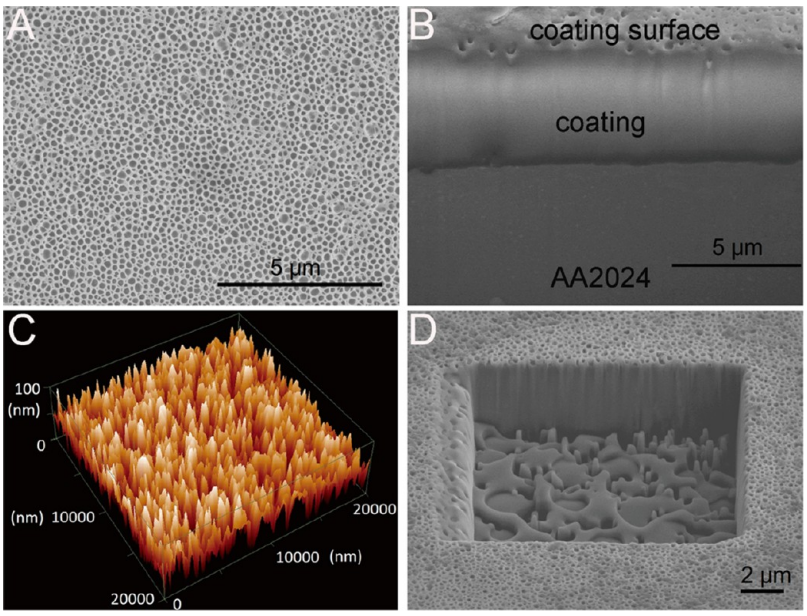

Figure 5. SEM images of (A) the surface, (B) the cross section, (C) AFM image of the smart nanocontainers doped SNAP coating; and (D) three-dimensional spatial distribution of the smart nanocontainers in the SNAP coating obtained by the FIB technique.

decreasing pH value, the release rate is noticeably accelerated. The release amount of caffeine under pH = 2 after immersion for 2 h is 5 times higher than that under pH = 5. It is not difficult to understand that according to the operation mechanism of the supramolecular nanovalves and diffusion regularity, the release rate of inhibitor molecules is dependent on the numbers of the opening nanovalves. The stronger the acidity is, the higher that is the degree of the protonation, the more recognition sites far away from mesopores orifices that are provided, and the more nanovalves that are opened.

The release study was also carried out under alkaline conditions and the release profiles shown in Figure 4C are similar to those in Figure 4B. The phenomenon of pH-dependent release rate under alkaline conditions is also observed. The stronger the alkalinity is, the higher the degree of the deprotonation of hexylammonium units is, the more numbers of CB[7] macrocycles dethread from the stalks there are, and the more supramolecular nanovalves that are opened. When the pH is adjusted to 10, the time required for releasing 70% of the total amount of caffeine molecules is only 80 min.

Overall, all the sorts of release characteristics of the synthesized mechanized HMSs, such as high loading capacity, acid and alkaline dual stimuli-responsive controlled release, zero release under neutral solution and initial burst release behavior, meet the requirement of the intelligent anticorrosion coatings for smart nanocontainers. In addition, the pH-dependent release rates ensure that if the mechanized HMSs as the smart nanocontainers are located in the severely corrosion microregions, in which pH values often deviate heavily from the neutral value, they can give a response of burst release of corrosion inhibitors and promptly reduce the corrosion rate.

Construction and Characterization of the Intelligent Anticorrosion Coating. A new sol−gel technology of the SNAP coating process, which includes two crucial steps of forming nanosized silica nanoparticles in suit and cross-linking the nanoparticles to produce a dense, protective thin film, has been put forward by the U.S. Air Force Research Laboratory and regarded as the environmentally friendly alternative to the chromate-based surface pretreatment on aircraft aluminum alloys.[48] Current SNAP coatings have been shown to generally offer an excellent physical barrier to corrosion for aluminum alloys; however, due to the lack of active components, such pretreatment coatings do not provide a self-healing ability when the coating suffers partial damage. In the present study, the mechanized HMSs as smart nanocontainers were incorporated into the SNAP coating in order to impart active anticorrosion ability. Figure 5A,B shows the top view and the cross-section SEM images of the smart nanocontainers doped SNAP coating. The thickness of the doped SNAP coating deposited on the AA2024 specimen is about 4.5 μm. We also notice that many microholes appear on the surface of all the two SNAP coatings (also see Figure S7A of Supporting Information), which is attributed to the rapid evaporation of cross-linking agents. The pretreatment surface structure is conductive to the subsequent adhesion of primer coatings. The smart nanocontainers doped SNAP coating is uniform, crack-free and the addition of the smart nanocontainers does not profoundly change the thickness of the coating as compared with the pure SNAP coating (Figure S7B of

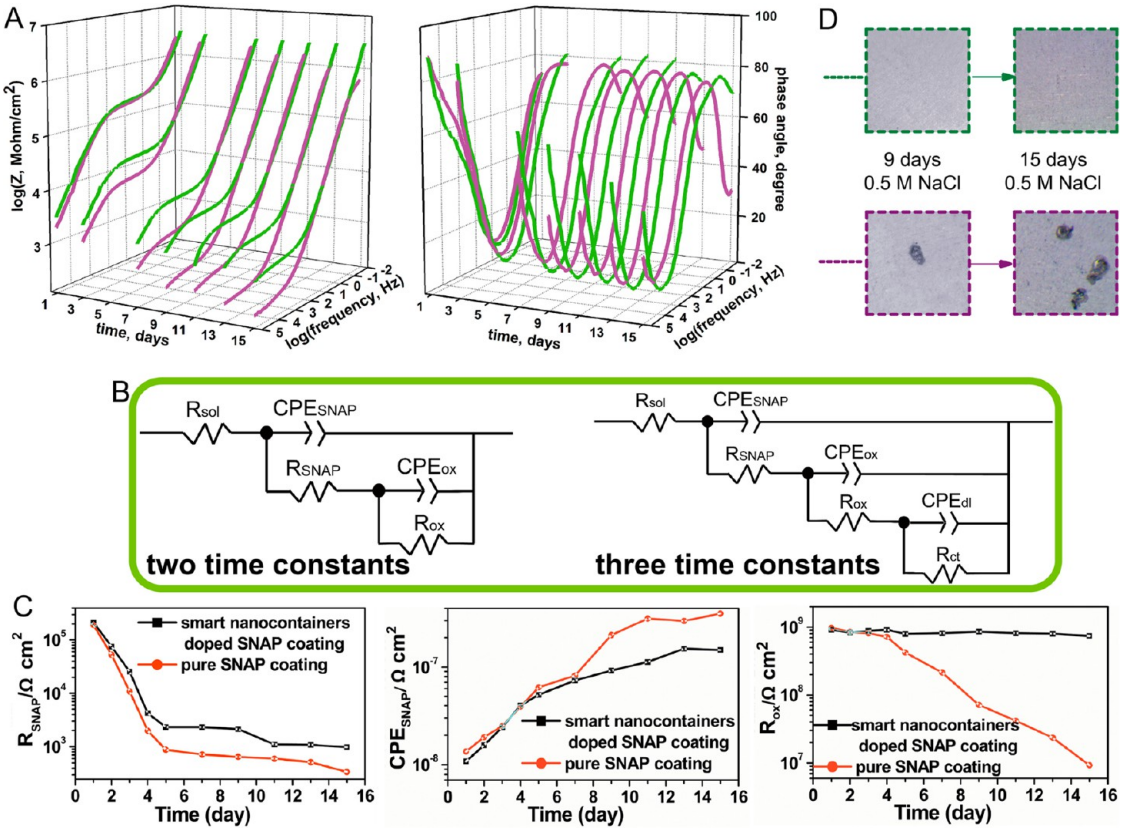

Figure 6. (A) Bode plots obtained on AA2024 coated with the pure SNAP coatings (red) and the smart nanocontainers doped SNAP coating (green) after immersion for 1, 3, 7, 9, 11, 13, 15 days in 0.5 M NaCl. (B) The equivalent circuits used for Bode plots fitting. (C) Evolution of R_{SNAP}, CPE_{SNAP} and R_{ox} obtained by fitting of bode plots using the appropriate equivalent circuits. (D) Optical observation of the pure SNAP coating and the smart nanocontainers doped SNAP coating after 9 days and 15 days of immersion in 0.5 M NaCl.

Supporting Information). AFM micrograph shown in Figure 5C manifests that the smart nanocontainers are distributed homogeneously over the surface of the SNAP coating, which leads to the result that the average surface roughness increases from 3.3 nm for the pure SNAP coating (Figure S7C of Supporting Information) to about 22.4 nm. To further clarify the spatial distribution of the smart nanocontainers within the SNAP coating, a defect with a 10 μm × 8 μm area was formed by the use of a focused ion beam, at 30 kV and 100 pA. In contrast to the flat open defect area of the pure SNAP coating (see Figure S7D of Supporting Information), some visibly uneven columns are formed by the difference of etching rate between the organosilicon components and the smart nanocontainers, which verifies the three-dimensional distribution of the smart nanocontainers.

Electrochemical Impedance Spectroscopy Evaluations. To quantitatively compare anticorrosion behaviors of the two different SNAP coatings and numerically interpret electrochemical phenomena on AA2024 surface, a nondestructive technique, electrochemical impedance spectroscopy (EIS) was adopted to provide the valuable information. Given the thickness of the coatings, EIS measurements were carried out in the high concentration of NaCl solution (0.5 M) in order to easily monitor the each stage of ongoing corrosion.

The evolutions of Bode plots with immersion time for the pure SNAP coating and the smart nanocontainers doped SNAP coating are shown in Figure 6A. At the beginning of immersion, the differences of the Bode plots between the two coatings are slight. Two well-defined time constants can be identified in the phase angle spectra. The high-frequency time constant is related to the capacitance of the passive SNAP coating, while the other time constant at low frequencies is attributed to the response of the aluminum oxide layer. An equivalent circuit (Figure 6B), consisting of two embedded RC circuits representing the SNAP coating/electrolyte (R_{SNAP}, pore resistance of the SNAP coating; CPE_{SNAP}, constant phase element of the SNAP coating) and aluminum oxide layer/SNAP coating (R_{ox}, resistance of the aluminum oxide layer; CPE_{ox}, constant phase element of oxide layer), is applied in this condition to extract the impedance data for analysis.

The resistance plateau between the two capacitive slopes represents the barrier property of passive coatings. With increased immersion time, the aggressive electrolyte species gradually penetrate pores of the SNAP coatings, resulting in the decrease of the

impedance modulus of SNAP coating and meaning the continued weakening of physical barrier effect. This trend is also proved by the decrease of R_{SNAP} and the increase of CPE_{SNAP} (see Figure 6C). Notably, the pore resistance of the smart nanocontainers doped SNAP coating is always half an order of magnitude higher than that of the pure SNAP coating during the early stage of immersion. Taking into account the almost identical thickness of the two coating samples, it can be concluded that the smart nanocontainers have good compatibility with the SNAP coating, and the uniformly distributed smart nanocontainers significantly reduce the porosity of the SNAP coating and prolong the physical barrier efficacy. However, the impedance modulus at the lowest frequency, $|Z|_{0.01\ Hz}$, which is also used to estimate the extent of corrosion activity,[49,50] remains generally stable for both two coatings, suggesting the aggressive species have not reached the alloy surface at this moment.

For immersion time up to ninth day, there are some substantial differences between the two coatings at low frequencies on the Bode plots. The pure capacitive behavior at low frequencies of the pure SNAP coating changes into the capacitive/resistive mixed behavior, accompanied by the appearance of the third time constant, which relates to the active corrosion processes.[51] The third time constant is attributed to the capacitance CPE_{dl} (constant phase element of double layer) and the resistance R_{ct} (charge transfer resistance), characterizing the onset of corrosion (Figure 6B). Conversely, for the smart nanocontainers doped SNAP coating, three important characteristics at low frequencies, including steady $|Z|_{0.01\ Hz}$ value, pure capacitive character, and no emergence of the third time constant, confirm that the aluminum oxide layer still keeps intact. The conclusion can be further verified by the optical microscopical observations (see Figure 6D). After 9 days of immersion, a few corrosion pits begin to appear on the pure SNAP coating; somewhat differently, the fresh and smooth surface is already clearly visible when the intelligent anticorrosion coating is deposited.

Aluminum oxide layer is a natural line of defense against corrosion; once broken, the metallic substrate will be directly exposed to the attack of the corrosive species. Therefore, R_{ox}, as a key indicator is often used to estimate the long-term anticorrosion performance of coatings and preliminary judge active anticorrosion properties.[52] Figure 6C also demonstrates the evolution of the R_{ox} for the two coatings during the whole immersion test. The R_{ox} for the pure SNAP coating remains relatively stable within the first few days, but after immersion for 4 days, it decreases rapidly, and at the end of the immersion, the R_{ox} falls to $9.27 \times 10^6\ \Omega\ cm^2$, which is 2 orders of mangnitude lower than the initial value. For comparison, the R_{ox} for the smart nanocontainers doped SNAP coating experiences slight fluctuation and then tends toward stability until the end of the immersion. There is no doubt that the incorporated smart nanocontainers stabilize the R_{ox}. As discussed above, the incorporation of the smart nanocontainers is not enough to stop the invasion of the corrosive species for a long time. When electrolyte species reach the alloy surface and corrosion occurs, the intelligent anticorrosion coating fully displays the self-healing ability and compensates the damaged oxide layer by coating repair factors. Furthermore, the smart nanocontainers, with the characteristics of high loading capacity and zero premature release under neutral solution, offer coating repair factors to full extent, and at the same time prevent their uncontrollable leaching, effectively extending the duration of the self-healing property, which is key for the intelligent anticorrosion coating to maintain no obvious pits and corrosion products after 15 days of immersion (see Figure 6D).

Scanning Vibrating Electrode Technique Measurements. To further validate the positive role of the smart nanocontainers in the self-healing process, the scanning vibrating electrode technique (SVET) was employed to monitor the changing trends of local current density surrounding artificial defects on the coatings at a microscopic level. The coatings were cross-scratched (3 mm long, 45 μm width) as shown in Figure 7A,B to easily detect the corrosion current during immersion in 0.1 M NaCl solution.

The evolutions of the 3D current density maps are depicted in Figure 7C−H for the two coatings after 1, 4, and 16 h of immersion. Both anodic current density corresponding to the local dissolution of the alloy matrix and cathodic corrosion activity relating to the reduction of dissolved oxygen in the defects on AA2024 coated with the pure SNAP coating are observed after only 1 h of immersion. With increasing immersion time, the anodic current density continues to grow. The cathodic current density is relatively low and remains this level for long-time immersion. These observations reveal the initiation and propagation of corrosion in the defects. In the case of the smart nanocontainers doped SNAP coating, a different type of evolution situation takes place. No corrosion signal appears after 1 h immersion. However, corrosion is detected after 4 h, which is observed as anodic peak of about 1.9 $\mu A\ cm^{-2}$ at the center of the defect area and some weak cathodic corrosion activity on the edge. Delightedly, since then the spreading of corrosion has been gradually controlled, and the measured current density demonstrates a significant decrease, even to a noisy level. After 16 h immersion, as can be seen from Figure 7H, the surface presents no remarkable electrochemical activity, which is in sharp contrast to the pure SNAP coating (Figure 7E), suggesting that all the corrosion activities are suppressed by self-healing functionality.

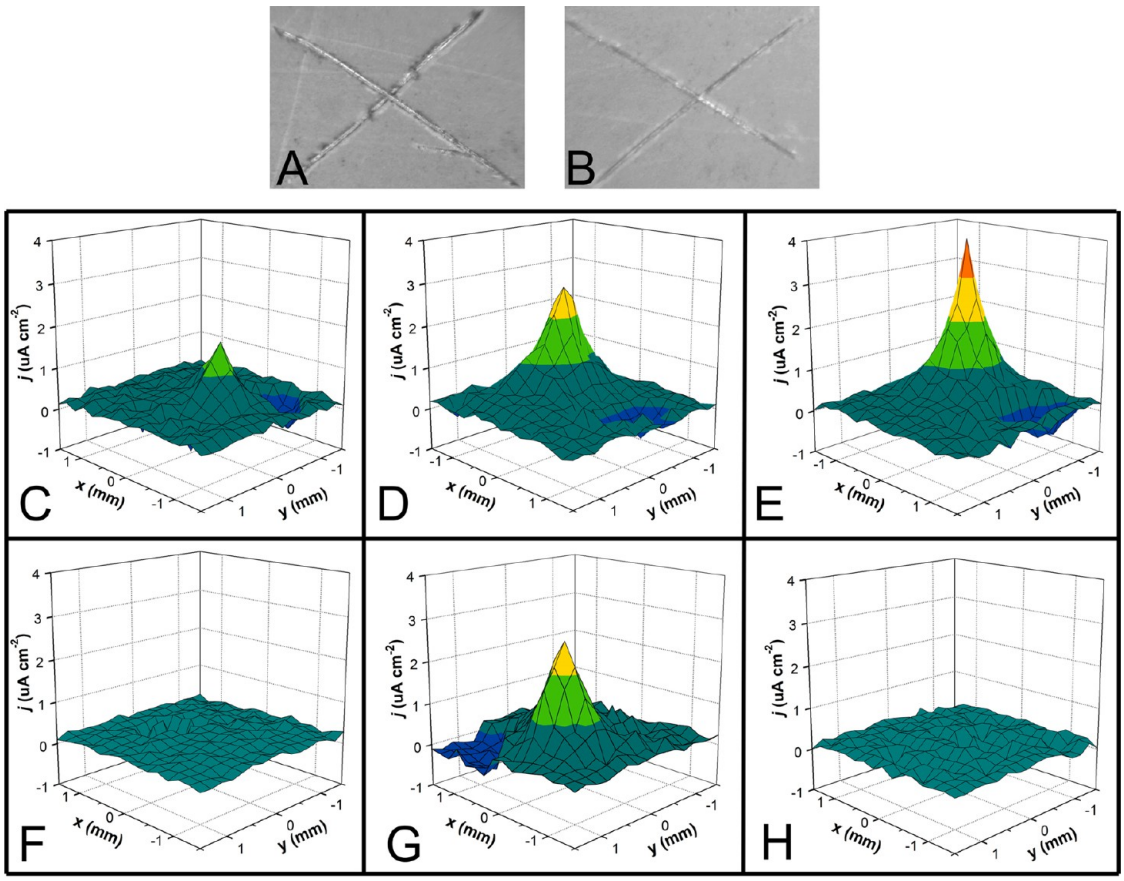

Figure 7. Optical images after 16 h of immersion in 0.1 M NaCl of AA2024 coated with (A) the pure SNAP coating and (B) the smart nanocontainers doped SNAP coating; (C−H) SVET current density maps after 1 h (C, F), 4 h (D, G) and 16 h (E, H) of immersion in 0.1 M NaCl for the pure SNAP coatings (middle) and the smart nanocontainers doped SNAP coating (bottom).

When AA2024 substrate undergoes corrosion in electrolyte solution, a number of microanodic and microcathodic regions will be emerged on the metallic surface. In the microanodic regions, the dissolution of aluminum and subsequent hydrolysis of aluminum ion lead to the decrease of pH and cause local acidification sites, while in the microcathodic regions, the oxygen reduction and possible proton reduction processes result in the pH elevation and local alkalization sites formation.[9,52] It can be inferred that the dispersed or the embedded smart nanocontainers congregated either in microanodic or in microcathodic regions are able to autonomously feel the abrupt change of pH and quickly give a response to release the caffeine molecules due to their acid and alkaline dual stimuli-responsive release characteristics. The released caffeine molecules protect the alloy surface from corrosion by forming molecular film on the damaged alloy surface, preventing the diffusion of aggressive species and oxygen to the scratched area. As caffeine is a coating repair factor, the efficient operation of caffeine molecules is also an important reason for the absence of corrosion activities after long-time immersion. When the smart nanocontainers without loading any inhibitor molecules are implanted into SNAP coating for comparison (see Figure S8), the evolutional tendency is very similar to that of the pure SNAP coating, and the phenomenon of self-healing is not observed during the investigated process.

CONCLUSIONS

In this work, the intelligent anticorrosion coating, constructed with the key component of the supramolecular self-assembly mechanized HMSs as smart nanocontainers and the basic framework of SNAP coating, is introduced. Experimental results prove that the smart nanocontainers are crucial to the intelligent anticorrosion effects. The advantages of the smart nanocontainers are centered on the following three points. (i) The smart nanocontainers have good compatibility with the SNAP coating, which is the basic requirement to implement anticorrosion task. (ii) Using HMSs as nanocarriers greatly increases the adsorption capacity of the coating repair factors, corrosion inhibitors, which provide the guarantee to the intelligent anticorrosion coating for durable self-healing capability. (iii) The CB[7]-based bistable pseudorotaxanes as supramolecular nanovalves achieve the acid and alkaline dual stimuli-responsive controlled release for corrosion inhibitors. The smart nanocontainers are

stimulated to activate the corrosion inhibiting action only when corrosion occurs. In summary, the delicate design of the intelligent anticorrosion coating integrates the excellent physical barrier property with the self-healing functionality, extends the lifetime of underlying alloy, and has a bright prospective in the future.

EXPERIMENTAL SECTION

Materials. Coupons of aluminum alloy AA2024 in the form of 1 cm × 4 cm × 0.04 cm were provided by XuSheng Co., (Nanjing, China). Tetraethylorthosilicate (TEOS), chloromethyltrimethoxysilane (CMTES), 1,6-hexanediamine (HDA), [2-(acryloyloxy)ethyl] trimethylammonium chloride (AETAC, 80 wt % in water), cetyltrimethylammonium bromide (CTAB), 2′2-azobis-(2-methylpropionamidine) dihydrochloride (V-50), 4-dimethylaminopyridine (DMAP), triethylene tetramine (TETA), cucurbit-[7]uril (CB[7]), caffeine, and (3-glycidyloxypropyl) trimethoxysilane (GPTMS) were purchased from Sigma-Aldrich. Ferrocene dicarboxylic acid (FCDCA) was obtained from J&K Scientific Co., Ltd. (Shanghai, China). All other reagents were of analytical grade and used as received. All the solutions were prepared using the deionized (DI) water (18.2 MΩ cm) originated from the Millipore Milli-Q water purification system.

Preparation and Functionalization of Hollow Mesoporous Silica Nanoparticles. Hollow mesoporous silica nanoparticles (HMSs) were prepared according to the reported method with minor modification. Briefly, the monodispersed polystyrene latex (PS) templates were synthesized first.[53] Ten milliliters of a 9 wt % PS aqueous solution was introduced dropwise to the mixture solution of CTAB (0.8 g), H_2O (29 mL), ethanol (15 mL) and ammonia solution (1 mL) under vigorous stirring at room temperature, followed by sonication for 15 min. Then, TEOS (1.34 mL) was added using an autosampler system within 5 min. After reaction for 48 h, the PS@CTAB/SiO_2 was collected by centrifugation and washed with ethanol. Finally, the obtained nanoparticles were calcined at 550 °C for 8 h. To completely remove the template and provide hydroxyl groups, the powder was reacted in ethanol/HCl mixture (5 mL HCl (37 wt %)/80 mL ethanol) at 50 °C for 5 h. The resulting HMSs were collected by centrifugation, washed thoroughly with MeOH, and then dried under vacuum.

The functionalization of HMSs included three steps. First, HMSs (200 mg) were dispersed in dry toluene (10 mL) under a nitrogen atmosphere. CMTES (60 mL, 0.28 mmol) was slowly added into the solution under magnetic stirring. After a refluxing step overnight, the CMTES-modified HMSs (HMSs-M1) were collected, washed with toluene and methanol, and then dried. Second, HMSs-M1 (100 mg) were dispersed ultrasonically in 10 mL of toluene containing excess amount of HAD. The mixture solution was refluxed overnight under nitrogen. Afterward, CMTES/HAD-modified HMSs (HMSs-M2) were recovered by centrifugation, washed with methanol, and dried. Finally, HMSs-M2 (100 mg) were dispersed in 10 mL of DMF, in which was dissolved FCDCA (100 μmol, 27 mg), followed by the addition of DCC (100 μmol, 27 mg) and DMAP (150 μmol, 20 mg). After they were stirred for 24 h under nitrogen, the resulting functionalized HMSs (HMSs-M3) were separated *via* centrifugation. To maximize the adsorption capacity, HMSs-M3 were sonicated in 5 mL of water for 5 h to remove DMF and unreacted FCDCA remained in mesopores, and then dried under vacuum in preparation for the next step.

Corrosion Inhibitor Loading, Capping, and Releasing Experiment. HMSs-M3 (50 mg) were added to 5 mL of PBS (pH = 7.4) containing caffeine (200 mg) and sonicated to dispersion. The suspended solution was stirred for 24 h under vacuum, after which it was in equilibrium at atmosphere for 4 h. To allow as many caffeine molecules as possible to diffuse into the hollow cavities of the HMSs, the above procedure was repeated three times. During the whole process, the temperature was maintained at 50 °C. The caffeine-loaded HMSs-M3 were obtained by centrifugation and dried under vacuum overnight. To entrap the caffeine, the CB[7] (50 mg), NaCl (5 mg) and caffeine (10 mg) were dissolved in 5 mL of PBS solution (pH =7.4), and then caffeine-loaded HMSs-M3 (50 mg) were added under stirring. The mixture solution was stirred for 3 days at room temperature to obtain the caffeine-loaded, CB[7]-capped HMSs-M3 (the mechanized HMSs). The mechanized HMSs were isolated by centrifugation, washed adequately with PBS solution (pH = 7.4), and dried under vacuum for further analysis and release experiment.

To investigate the amount of caffeine releasing from the mechanized HMSs at different pH values, the mechanized HMSs (1 mg) were placed in the dialysis bag at the top of the sealed quartz cuvette to avoid interference, and the desired pH solution (acidic, adjustment by HCl solution; neutral, PBS 6.5; alkaline, adjustment by NaOH solution) was carefully added into the cuvette to ensure the mechanized HMSs were completely immersed into the solution. The UV/vis absorbance of the dissolved caffeine was recorded at 1 s interval over the entire period of release experiments.

Construction and Anticorrosion Evaluations of the Intelligent Anticorrosion Coating. Coupons of AA2024 were abraded with emery paper to 1500 grit, degreased in acetone, sonicated in deionized water (40 kHz, 200 W, 15 min), etched in HNO_3 solution (20%, 10 min, 40 °C), rinsed with deionized water, and dried in the atmosphere.

Self-assembled nanophase particle (SNAP) sol was synthesized by hydrolyzing GPTMS and TEOS in a dilute solution of acetic acid solution (0.05 mol/L) controlling a molar ratio GPTMS/TEOS/water of 3:1:15. After the solution was aged in a sealed vial for 3 days, the SNAP sol with the addition of the appropriate amount of mechanized HMSs (2 mg/mL) was prepared for the intelligent anticorrosion coating. A SNAP sol without mechanized HMSs was also prepared as reference (the pure SANP coating). After ultrasonic dispersion for 30 s, TETA (n(GPTMS)/n(TETA) = 7.8:1) was added into the mechanized HMSs incorporated SNAP sol under stirring at room temperature within 1 min. The intelligent anticorrosion coating on the surface of AA2024 substrates was fabricated by a dip-coating procedure. The pretreated AA2024 coupon was immersed into the resulting sol for 120 s followed by withdrawal at a speed of 2 mm·s^{-1}. Finally, the samples were air-dried at 100 °C for 30 min.

Electrochemical impedance (EIS) measurements and potentiodynamic polarization studies were carried out using a PARSTAT 2273 potentiostat/galvanostat. A conventional three electrode cell in a Faraday cage was used, composed of a saturated calomel reference electrode (SCE), a platinum foil as the counter electrode, and the coated AA2024 substrates as the working electrodes (exposed area: 0.5 cm^2). Potentiodynamic polarization studies were swept from −250 to +250 mV with respect to the open circuit potential at a scan rate of 0.166 mV s^{-1}. EIS measurements were performed with applied 10 mV sinusoidal perturbations in the frequency range from 100 kHz to 10 mHz, with 10 points per decade. The impedance plots were fitted with the ZSimpWin software.

The SVET measurements were performed in 0.1 M NaCl solution using a M370 device (Princeton Applied Research). Prior to measurement, the artificial scratches were carefully created with a sharp needle to avoid damage the metal surface. The Pt-blackened electrode tip with a diameter of 20 μm and was situated 100 μm above the surface of the coatings. The electrode vibrated with a frequency of 75 Hz and the peak-to-peak amplitude was 30 μm. The defected areas of 3 mm × 3 mm were scanned with a step width of 200 μm which results in a 16 × 16-matrix. Experimental results are presented in the form of 3D maps of ionic currents. All the tests were conducted at the open-circuit potential.

Characterization. Fourier transform infrared spectra (FT-IR) were recorded on a Bruker Tensor 27 FTIR spectrometer. Scanning electron microscopy (SEM, S-4800, Hitachi) and transmission electron microscopy (TEM, JEM-2100, JEOL) were used to

examine the morphologies of the HMSs. HADDF STEM image and STEM EDX mapping were recorded from FEI-Tecnai F20 transmission electron microscope operated at 200 kV. Small-angle powder X-ray diffraction (XRD) patterns were recorded on a Bruker D8 Advanced diffractometer using Cu Kα radiation (λ = 1.5406 Å). The N_2 adsorption–desorption isotherms were obtained at 77 K on a Quanta chrome Nova 1000 Micrometric apparatus. The specific surface area was calculated by the Brunauer–Emmett–Teller (BET) method. The pore size and pore volume were calculated by the Barrett–Joyner–Halenda (BJH) method according to the adsorption branch of the isotherm. The solid state ^{13}C and ^{29}Si CPMAS NMR spectra were collected on a Bruker DSX400 NMR spectrometer, operating at Larmor frequencies of 100.6 and 79.5 MHz and equipped with a 7 mm probe. UV/vis measurements were performed using a Shimadzu UV-1800 spectrometer.

Conflict of Interest: The authors declare no competing financial interest.

Acknowledgment. This research was financially supported by the National Natural Science Foundation of China (No. 51102135), the Natural Science Foundation of Jiangsu Province (No. BK2011711), the 2013-ZiJin-0102 Talent Program, NUST, and Jiangsu Graduate Innovation Project (No. CXLX13_196).

Supporting Information Available: Assembly schematic diagram, FTIR spectra, TGA analysis, N_2 adsorption–desorption isotherm and pore size distribution, Tafel polarization curves, the characterizations of the pure SNAP coating and SVET current density maps. This material is available free of charge *via* the Internet at http://pubs.acs.org.

REFERENCES AND NOTES

1. Presuel-Moreno, F.; Jakab, M. A.; Tailleart, N.; Goldman, M.; Scully, J. R. Corrosion-Resistant Metallic Coatings. *Mater. Today* **2008**, *11*, 14–23.
2. Andreeva, D. V.; Shchukin, D. G. Smart Self-Healing Protective Coatings. *Mater. Today* **2008**, *11*, 24–30.
3. Hughes, A. E.; Cole, I. S.; Muster, T. H.; Varley, R. J. Designing Green, Self-Healing Coatings for Metal Protection. *NPG Asia Mater.* **2010**, *2*, 143–151.
4. Murphy, E. B.; Wudl, F. The World of Smart Healable Materials. *Prog. Polym. Sci.* **2010**, *35*, 223–251.
5. Cho, S. H.; White, S. R.; Braun, P. V. Self-Healing Polymer Coatings. *Adv. Mater.* **2009**, *21*, 645–649.
6. Shchukin, D. G.; Mohwald, H. Smart Nanocontainers as Depot Media for Feedback Active Coatings. *Chem. Commun.* **2011**, *47*, 8730–8739.
7. Shchukin, D. G.; Mohwald, H. Self-Healing Coatings Containing Active Nanoreservoirs. *Small* **2007**, *3*, 926–943.
8. Jakab, M. A.; Scully, J. R. On-Demand Release of Corrosion-Inhibiting Ions from Amorphous Al-Co-Ce Alloys. *Nat. Mater.* **2005**, *4*, 667–670.
9. Skorb, E. V.; Fix, D.; Andreeva, D. V.; Mohwald, H.; Shchukin, D. G. Surface-Modified Mesoporous SiO_2 Containers for Corrosion Protection. *Adv. Funct. Mater.* **2009**, *19*, 2373–2379.
10. Li, G. L.; Zheng, Z. L.; Mohwald, H.; Shchukin, D. G. Silica/Polymer Double-Walled Hybrid Nanotubes: Synthesis and Application as Stimuli-Responsive Nanocontainers in Self-Healing Coatings. *ACS Nano* **2013**, *7*, 2470–2478.
11. Skorb, E. V.; Skirtach, A. G.; Sviridoc, D. V.; Shchukin, D. G.; Mohwald, H. Laser-Controllable Coatings for Corrosion Protection. *ACS Nano* **2009**, *3*, 1753–1760.
12. Skorb, E. V.; Sviridov, D. V.; Mohwald, H.; Shchukin, D. G. Light Responsive Protective Coatings. *Chem. Commun.* **2009**, *40*, 6041–6043.
13. Tedim, J.; Zheludkevich, M. L.; Salak, A. N.; Lisenkov, A.; Ferreira, M. G. S. Nanostructured LDH-Container Layer with Active Protection Functionality. *J. Mater. Chem.* **2011**, *21*, 15464–15470.
14. Borisova, D.; Mohwald, H.; Shchukin, D. G. Mesoporous Silica Nanoparticles for Active Corrosion Protection. *ACS Nano* **2011**, *5*, 1939–1946.
15. Haase, M. F.; Grigoriev, D. O.; Mohwald, H.; Shchukin, D. G. Development of Nanoparticle Stabilized Polymer Nanocontainers with High Content of the Encapsulated Active Agent and Their Application in Water-Borne Anticorrosive Coatings. *Adv. Mater.* **2012**, *24*, 2429–2435.
16. Lvov, Y. M.; Shchukin, D. G.; Mohwald, H.; Price, R. R. Halloysite Clay Nanotubes for Controlled Release of Protective Agents. *ACS Nano* **2008**, *2*, 814–820.
17. Zheludkevich, M. L.; Shchukin, D. G.; Yasakau, K. A.; Mohwald, H.; Ferreira, M. G. S. Anticorrosion Coating with Self-Healing Effect Based on Nanocontainers Impregnated with Corrosion Inhibitor. *Chem. Mater.* **2007**, *19*, 402–411.
18. Shchukin, D. G.; Mohwald, H. Surface-Engineered Nanocontainers for Entrapment of Corrosion Inhibitors. *Adv. Funct. Mater.* **2007**, *17*, 1451–1458.
19. Andreeva, D. V.; Skorb, E. V.; Shchukin, D. G. Layer-by-Layer Polyelectrolyte/Inhibitor Nanostructures for Metal Corrosion Protection. *ACS Appl. Mater. Interfaces* **2010**, *2*, 1954–1962.
20. Grigoriev, D. O.; Kohler, K.; Skorb, E.; Shchukin, D. G.; Mohwald, H. Polyelectrolyte Complexes as a "Smart" Depot for Self-healing Anticorrosion Coatings. *Soft Matter* **2009**, *5*, 1426–1432.
21. Hollamby, M. J.; Fix, D.; Donch, I.; Borisova, D.; Mohwald, H.; Shchukin, D. G. Hybrid Polyester Coating Incorporating Functionalized Mesoporous Carriers for the Holistic Protection of Steel Surfaces. *Adv. Mater.* **2011**, *23*, 1361–1365.
22. Zheng, Z. L.; Huang, X.; Schenderlein, M.; Borisova, D.; Cao, R.; Mohwald, H.; Shchukin, D. G. Self-Healing and Antifouling Multifunctional Coatings Based on pH and Sulfide Ion Sensitive Nanocontainers. *Adv. Funct. Mater.* **2013**, *23*, 3307–3314.
23. Snihirova, D.; Lamaka, S. V.; Taryba, M.; Salak, A. N.; Kallip, S.; Zheludkevich, M. L.; Ferreira, M. G. S.; Motemor, M. F. Hydroxyapatite Microparticles as Feedback-Active Reservoirs of Corrosion Inhibitors. *ACS Appl. Mater. Interfaces* **2010**, *2*, 3011–3022.
24. Zheludkevich, M. L.; Tedim, J.; Freire, C. S. R.; Fernandes, S. C. M.; Kallip, S.; Lisenkov, A.; Gandini, A.; Ferreira, M. G. S. Self-Healing Protective Coatings with "Green" Chitosan Based Pre-Layer Reservoir of Corrosion Inhibitor. *J. Mater. Chem.* **2011**, *21*, 4805–4812.
25. Shchukin, D. G. Container-Based Multifunctional Self-Healing Polymer Coatings. *Polym. Chem.* **2013**, *4*, 4871–4877.
26. Badjic, J. D.; Balzani, V.; Credi, A.; Silvi, S.; Stoddart, J. F. A Molecular Elevator. *Science* **2004**, *303*, 1845–1849.
27. Wang, C.; Li, Z. X.; Cao, D.; Zhao, Y. L.; Gaines, J. W.; Bozdemir, O. A.; Ambrogio, M. W.; Frasconi, M.; Botros, Y. Y.; Zink, J. I.; *et al.* Stimulated Release of Size-Selected Cargos in Succession from Mesoporous Silica Nanoparticles. *Angew. Chem., Int. Ed.* **2012**, *51*, 5460–5465.
28. Xue, M.; Zhong, X.; Shaposhnik, Z.; Qu, Y. Q.; Tamanoi, F.; Duan, X. F.; Zink, J. I. pH-Operated Mechanized Porous Silicon Nanoparticles. *J. Am. Chem. Soc.* **2011**, *133*, 8798–8801.
29. Zhao, Y. L.; Li, Z. X.; Kabehie, S.; Botros, Y. Y.; Stoddart, J. F.; Zink, J. I. pH-Operated Nanopistons on the Surface of Mesoporous Silica Nanoparticles. *J. Am. Chem. Soc.* **2010**, *132*, 13016–13025.
30. Khashab, N. M.; Trabolsi, A.; Lau, Y. A.; Ambrogio, M. W.; Friedman, D. C.; Khatib, H. A.; Zink, J. I.; Stoddart, J. F. Redox- and pH-Controlled Mechanized Nanoparticles. *Eur. J. Org. Chem.* **2009**, *11*, 1669–1673.
31. Lai, J. P.; Shah, B. P.; Garfunkel, E.; Lee, K. B. Versatile Fluorescence Resonance Energy Transfer-Based Mesoporous Silica Nanoparticles for Real-Time Monitoring of Drug Release. *ACS Nano* **2013**, *7*, 2741–2750.
32. Kim, H.; Kim, S.; Park, C.; Lee, H.; Park, H. J.; Kim, C. Glutathione-Induced Intracellular Release of Guests from Mesoporous Silica Nanocontainers with Cyclodextrin Gatekeepers. *Adv. Mater.* **2010**, *22*, 4280–4283.
33. Sun, Y. L.; Yang, B. J.; Zhang, S. X. A.; Yang, Y. W. Cucurbit-[7]uril Pseudorotaxane-Based Photoresponsive Supramolecular Nanovalve. *Chem.—Eur. J.* **2012**, *18*, 9212–9216.

34. Yan, H.; The, C.; Sreejith, S.; Zhu, L. L.; Kwok, A.; Fang, W. Q.; Ma, X.; Nguyen, K. T.; Korzh, V.; Zhao, Y. L. Functional Mesoporous Silica Nanoparticles for Photothermal-Controlled Drug Delivery *in Vivo*. *Angew. Chem., Int. Ed.* **2012**, *51*, 8373–8377.
35. Patel, K.; Angelos, S.; Dichtel, W. R.; Coskun, A.; Yang, Y. W.; Zink, J. I.; Stoddart, J. F. Enzyme-Responsive Snap-Top Covered Silica Nanocontainers. *J. Am. Chem. Soc.* **2008**, *130*, 2382–2383.
36. Sun, Y. L.; Zhou, Y.; Li, Q. L.; Yang, Y. W. Enzyme-Responsive Supramolecular Nanovalves Crafted by Mesoporous Silica Nanoparticles and Choline-Sulfonatocalix[4]arene[2] Pseudorotaxanes for Controlled Release. *Chem. Commun.* **2013**, *49*, 9033–9035.
37. Ambrogio, M. W.; Thomas, C. R.; Zhao, Y. L.; Zink, J. I.; Stoddart, J. F. Mechanized Silica Nanoparticles: A New Frontier in Theranostic Nanomedicine. *Acc. Chem. Res.* **2011**, *44*, 903–913.
38. Tarn, D.; Ashley, C. E.; Xue, M.; Cames, E. C.; Zink, J. I.; Brinker, C. J. Mesoporous Silica Nanoparticle Nanocarriers: Biofunctionality and Biocompatibility. *Acc. Chem. Res.* **2013**, *46*, 792–801.
39. Chen, T.; Fu, J. J. An Intelligent Anticorrosion Coating based on pH-Responsive Supramolecular Nanocontainers. *Nanotechnology* **2012**, *23*, 505750.
40. Chen, T.; Fu, J. J. pH- Responsive Nanovalves based on Hollow Mesoporous Silica Spheres for Controlled Release of Corrosion Inhibitor. *Nanotechnology* **2012**, *23*, 235605.
41. Chen, T.; Yang, N. W.; Fu, J. J. Controlled Release of Cargo Molecules from Hollow Mesoporous Silica Nanoparticles Based on Acid and Base Dual-Responsive Cucurbit[7]uril Pseudorotaxanes. *Chem. Commun.* **2013**, *49*, 6555–6557.
42. Angelos, S.; Yang, Y. W.; Patel, K.; Stoddart, J. F.; Zink, J. I. pH-Responsive Supramolecular Nanovalves Based on Cucurbit[6]uril Pseudorotaxanes. *Angew. Chem., Int. Ed.* **2008**, *47*, 2222–2226.
43. Liu, J. S.; Du, X. Z. pH- and Competitor-Driven Nanovalves of Cucurbit[7]uril Pseudorotaxanes Based on Mesoporous Silica Supports for Controlled Release. *J. Mater. Chem.* **2010**, *20*, 3642–3649.
44. Kim, Y.; Kim, H.; Ko, Y. H.; Selvapalam, N.; Rekharsky, M. V.; Inoue, Y.; Kim, K. Complexation of Aliphatic Ammonium Ions with a Water-Soluble Cucurbit[6]uril Derivative in Pure Water: Isothermal Calorimetric, NMR, and X-Ray Crystallographic Study. *Chem.—Eur. J.* **2009**, *15*, 6143–6151.
45. Chen, Y.; Chen, H. R.; Guo, L. M.; He, Q. J.; Chen, F.; Zhou, J.; Feng, J. W.; Shi, J. L. Hollow/Rattle Type Mesoporous Nanostructures by a Structural Difference-Based Selective Etching Strategy. *ACS Nano* **2010**, *4*, 529–539.
46. Lou, X. W.; Archer, L. A.; Yang, Z. C. Hollow Micro-/Nanostructures: Synthesis and Application. *Adv. Mater.* **2008**, *20*, 3987–4019.
47. Tang, F. Q.; Li, L. L.; Chen, D. Mesoporous Silica Nanoparticles: Synthesis, Biocompatibility and Drug Delivery. *Adv. Mater.* **2012**, *24*, 1504–1534.
48. Zheludkevich, M. L.; Salvado, I. M.; Ferreira, M. G. S. Sol-Gel Coatings for Corrosion Protection Metals. *J. Mater. Chem.* **2005**, *15*, 5099–5111.
49. Borisova, D.; Mohwald, H.; Shchukin, D. G. Influence of Embedded Nanocontainers on the Efficiency of Active Anticorrosive Coatings for Aluminum Alloys Part I: Influence of Nanocontainer Concentration. *ACS Appl. Mater. Interfaces* **2012**, *4*, 2931–2939.
50. Borisova, D.; Mohwald, H.; Shchukin, D. G. Influence of Embedded Nanocontainers on the Efficiency of Active Anticorrosive Coatings for Aluminum Alloys Part II: Influence of Nanocontainer Position. *ACS Appl. Mater. Interfaces* **2013**, *5*, 80–87.
51. Maia, F.; Tedim, J.; Lisenkov, A. D.; Salak, A. N.; Zheludkevich, M. L.; Ferreira, M. G. S. Silica Nanocontainers for Active Corrosion Protection. *Nanoscale* **2012**, *4*, 1287–1298.
52. Lamaka, S. V.; Shchukin, D. G.; Andreeva, D. V.; Zheludkevich, M. L.; Mohwald, H.; Ferreira, M. G. S. Sol-Gel/Polyelectrolyte Active Corrosion Protection System. *Adv. Funct. Mater.* **2008**, *18*, 3137–3147.
53. Qi, G. G.; Wang, Y. B.; Estevez, L.; Switzer, A. K.; Duan, X. N.; Yang, X. F.; Giannelis, E. P. Facile and Scalable Synthesis of Monodispersed Spherical Capsules with a Mesoporous Shell. *Chem. Mater.* **2010**, *22*, 2693–2695.